Time and Frequency Blanking for Radio-Frequency Interference Mitigation in Microwave Radiometry

Barış Güner, Joel T. Johnson, *Senior Member, IEEE*, and Noppasin Niamsuwan, *Member, IEEE*

***Abstract*—Radio-frequency interference (RFI) is a major limiting factor in passive microwave remote sensing and radio astronomy. A digitally based radiometer system has been developed to improve RFI mitigation through the use of high temporal and spectral resolution. The system includes a pulse-blanking algorithm that is capable of removing pulsed time-domain sources in real time. Cross-frequency mitigation is also possible in postprocessing through the use of the system's high spectral resolution. Several experiments have been conducted at L- and C-bands in recent years. Datasets from two particular campaigns are analyzed in this paper: ground-based observations at L-band in Canton, Michigan that emphasize pulse blanking and an airborne campaign at C-band over Texas and the Gulf of Mexico that emphasizes cross-frequency mitigation. Results and analyses are presented to quantify the RFI mitigation performance achieved.**

***Index Terms*—Microwave radiometry, radio-frequency interference (RFI).**

I. Introduction

RECENT measurements with spaceborne Earth observing radiometers have shown significant corruption of C-band brightness temperatures due to radio-frequency interference (RFI) [1], [2]. Since there is no portion of the C-band spectrum for which transmissions are prohibited, microwave radiometers operating in this band for sensing soil moisture, sea surface temperature, or other geophysical parameters require a means to mitigate RFI. At L-band, although the frequency range of 1400–1427 MHz is protected, RFI sources operating very close to these frequencies may still degrade radiometric measurements. Also, operation in a bandwidth larger than the protected 27 MHz is desirable, if possible, to increase the sensitivity of the radiometer to geophysical parameters. While the detection and mitigation of RFI is an important issue for radiometry in general, C- and L-bands are of particular interest at present due to their use in current and future systems.

Many current RFI mitigation techniques rely on the facts that RFI always increases the observed brightness beyond that due to thermal noise alone and that anthropogenic emissions are almost always localized in time or frequency. Therefore, if sufficient temporal or spectral resolution is obtained, it is possible to distinguish unnatural increases in brightness caused by time- or frequency-localized RFI sources [3]–[5]. Other RFI detection strategies have also been proposed based on examination of the statistics of the received fields [6], but such approaches are not considered here. The use of digitally based receiver hardware as compared to traditional analog systems is advantageous for RFI detection and mitigation due to a digital receiver's inherently high temporal sampling rate and ability to obtain a large number of frequency channels with little additional complexity. With these goals in mind, digitally based radiometers have been under investigation at The Ohio State University ElectroScience Laboratory since 2002 [7]. The systems developed have successfully performed in several airborne and ground-based demonstrations at L- and C-bands [8]–[12]. Henceforth, the version of the digital radiometer utilized for L-band observations is called the L-band interference suppressing radiometer (LISR), while the version used at C-band is called the C-band interference suppressing radiometer (CISR). Both systems include a real-time pulse-blanking algorithm [called asynchronous pulse blanking (APB) in what follows] implemented in digital hardware, and both achieve high frequency resolution through a fast Fourier transform (FFT) operation again performed in digital hardware. The latter allows the mitigation of frequency-localized sources through postprocessing analyses.

In this paper, the mitigation performance that is achieved by time- and frequency-domain blanking is assessed. A discussion of time-domain blanking follows in Section II through the use of data obtained from an L-band ground-based campaign in Canton, Michigan [8]. This campaign was performed in close proximity to a pulsed radar system operating at a frequency close to the radiometer's passband and, hence, is useful for showing the effectiveness of the APB algorithm. Results from an airborne campaign at C-band over Texas and the Gulf of Mexico [11] are described in Section III and are used to examine the effectiveness of frequency-domain blanking in a complex RFI environment. Final conclusions and discussions are provided in Section IV.

II. L-Band Observations of an Air-Route Surveillance Radar (ARSR) System in Canton, MI

Data from a ground-based campaign involving L-band observations in close proximity to an ARSR located in Canton, MI, on June 16 and 17, 2005 are used to demonstrate RFI mitigation in the time domain. This campaign (which will be denoted as the Canton campaign) was conducted by researchers from the University of Michigan [6], NASA Goddard Space Flight Center [13], and The Ohio State University, and included

Manuscript received March 15, 2007; revised May 24, 2007.

The authors are with the Department of Electrical and Computer Engineering and ElectroScience Laboratory, The Ohio State University, Columbus, OH 43210 USA (e-mail: guner.2@osu.edu; johnson.1374@osu.edu).

Color versions of one or more of the figures in this paper are available online at http://ieeexplore.ieee.org.

Digital Object Identifier 10.1109/TGRS.2007.903680

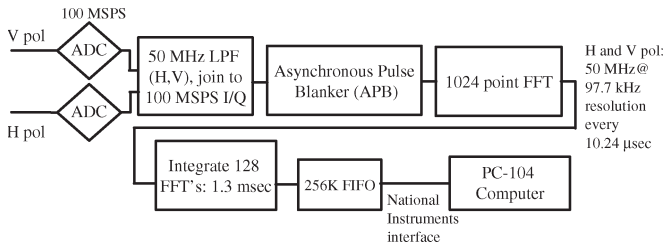

Fig. 1. LISR block diagram.

advanced RFI mitigating radiometer "backends" from each of these organizations. A truck-mounted L-band radiometer front end supplied by the University of Michigan was placed within approximately 200 m of the ARSR antenna, ensuring that strong out-of-band interference would be experienced in the observations. The experiment was designed to demonstrate that the backends developed could successfully remove interference in both extremely strong and slight interference environments. The latter case was obtained through a choice of the observation direction of the radiometer antenna, as well as the fact that the radar center frequency (reported as 1315 MHz by the station's literature) was far out of band of the radiometer observations. Other properties of the radar reported by the station are a peak radiated power of 4 MW, an antenna gain of 35 dB, an antenna tilt angle of 2.6°, a typical pulse repetition frequency (PRF) of 360 Hz, and a pulsewidth of 2 μs.

A. *Instrumentation*

The L-band radiometer front end contained dual receivers so that simultaneous observations of horizontal and vertical polarization were provided. The system utilized a large L-band horn antenna with a half-power beamwidth of 20° and included internal calibration standards so that the antenna temperature could be directly computed from the measured data. Results will be reported as calibrated antenna temperatures, not the brightness temperature of the observed scene, as external calibration standards were not available in the campaign. The use of the antenna temperature rather than the scene brightness temperature is not expected to have any significant impact on an assessment of RFI mitigation performance.

RF filters within the radiometer front end set the RF 3-dB bandwidth from 1403.5 to 1423.5 MHz. The RF signal is downconverted with a local oscillator (LO) at either 1386.5 or 1440.5 MHz such that an intermediate frequency (IF) bandwidth of 17–37 MHz is obtained; image rejection in the downconversion process is provided by the RF front-end filters. IF outputs for both polarizations were then power-divided and supplied to the three backend systems.

A block diagram of LISR as configured for this experiment is provided in Fig. 1. LISR samples both the incoming H- and V-pol 17–37 MHz IFs at 100 MSPS using 10-bit analog-to-digital (A/D) converters for this purpose. The subsequent LISR operations described in Fig. 1 take place in a single field-programmable gate array (FPGA). First, the incoming IFs are digitally filtered and then combined into a single complex datastream at 100 MSPS. The digital filter used has a bandwidth wider than that set by the RF filters and, therefore, has little

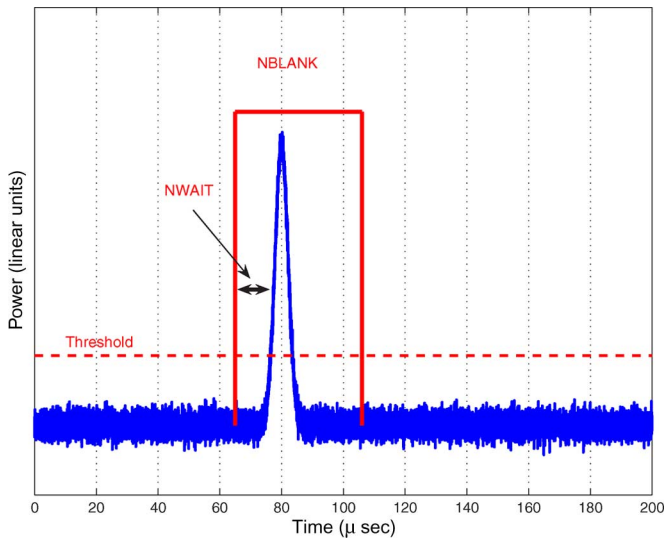

Fig. 2. Basic operation procedure of APB.

impact on the measured data. However, its use allows removal of the image spectrum for each of the input polarizations so that the combination into a single 100-MSPS complex datastream is possible.

Following this output is a set of processors that can be controlled by the operator in real time through an Ethernet interface between the system computer and the FPGA. In the results presented here, LISR was operated in three distinct modes, which are labeled as "Integration, APB off," "Integration, APB on," and "Capture" in what follows.

In "Capture" mode, the 100-MSPS complex datastream is directly passed to the control and recording computer without further processing. The high temporal resolution and coherent data acquired allow detailed studies of the properties of the observed interference. Results from this mode are not presented here, but are available in [8].

The other LISR modes utilize data that have passed through the APB stage. The APB is designed to detect and blank radar pulses in real time so that their effects can be removed without further processing while maintaining accurate calibration of the noise-free data [14]. The basic operation principle of the APB is illustrated in Fig. 2. To detect pulsed interferers, the APB maintains a running estimate of the mean and variance of the incoming power in the time domain (through the use of an exponential averaging operation as described in [14]). Whenever a sample power greater than a threshold number of standard deviations from the mean is detected, the APB blanks (sets to zero) a block of samples of length NBLANK beginning from a predetermined period before the triggering sample (shown as NWAIT in the figure) through and hopefully including any multipath components associated with the detected pulses. APB operating parameters are adjustable and can be set by the user. In the experiments described here, the APB threshold was set to nine standard deviations from the mean power level, and a blanking window of 40 μs was used (note that 40 μs corresponds to 6 km of radar range.) This window began 10.24 μs prior to the detected sample. The APB provides information on the amount of blanking to further processor stages so that blanking effects on calibration can be corrected in real time.

The expected false-alarm rate (i.e., fraction of samples blanked when the input fields are RFI-free Gaussian noise) of the APB processor can ideally be determined analytically as a function of the detection threshold and other APB parameters. Given the Nyquist sampled complex datastream input to the APB, individual sample powers are exponential random variables, and the probability of exceeding the mean power by a specified number of standard deviations can easily be determined. However, the APB processor also controls the number of blanking "windows" that can be created within a specified time period, as described in [14], making analytical evaluation of the false-alarm rate difficult. Monte Carlo simulations of the APB processor were instead utilized to determine that 1.6% of samples were blanked under RFI-free conditions for the APB parameters of the Canton campaign; this result was found consistent with the percent blanking observed for the internal calibration standards in the experiment. Again, the effect of blanking is compensated for when computing averages, as described in [14], and laboratory results confirm that average RFI-free brightnesses are unaffected by the blanking process. Further reduction in the false alarm rate of the detector can be achieved by incorporating a pre-detection integration of the observed power, but is not considered here.

Following the APB is a length 1K complex FFT utilizing a triangular window to reduce truncation effects. This FFT operation provides an output every 10.24 μs, with two sets of 512 bins obtained in two corresponding 50-MHz bandwidths; the first set is for horizontal, and the second set for vertical polarization. The resulting spectral resolution is approximately 97 kHz, which is much finer than the bandwidth of many expected RFI sources. FFT outputs are then passed through detection and integration operations, with the final datastream comprised of 1024 frequency bins obtained every 1.3 ms.

The distinction between "Integration, APB on" and "Integration, APB off" modes involves whether the APB blanking is turned ON or OFF in the data input to the FFT operation. Comparing the brightnesses obtained in these modes allows the effectiveness of the APB real-time pulse removal algorithm to be examined. Results following integration are stored in a 32-bit 256-K FIFO and then passed through a National Instruments interface to the system control computer. The basic antenna observations consisted of 205 spectra (262.4-ms integration time) acquired and transferred to the system computer before the front end switched to internal load observations.

B. Time-Domain Blanking Results

Strong and weak RFI cases were produced in the campaign by changing the observation direction of the antenna; the radar was located at an azimuth angle of approximately 160° with respect to the default position of the antenna. Therefore, the data obtained at azimuthal observation angles of 0° and 160° will be compared to show the effectiveness of the APB algorithm in the "weak" and "strong" cases, respectively. In both cases, the elevation angle of the antenna was 1°.

Figs. 3 and 4 plot the calibrated antenna temperatures in vertical and horizontal polarizations, respectively, for both "Integration, APB on" and "Integration, APB off" modes when

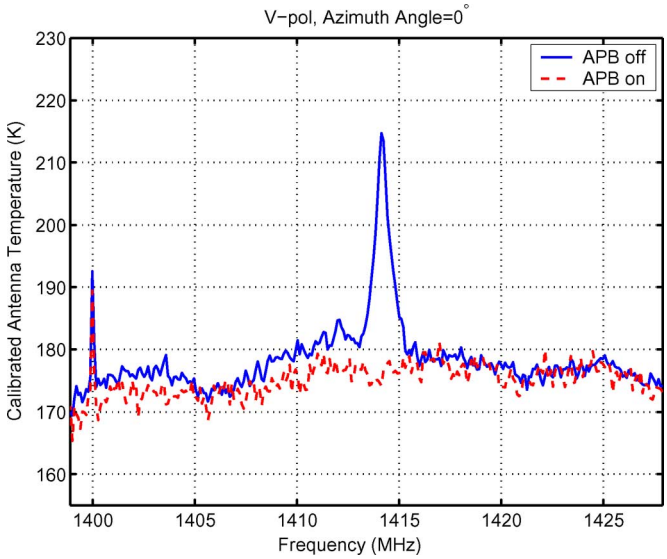

Fig. 3. Average calibrated antenna temperature versus frequency, V-pol, azimuth angle = 0°.

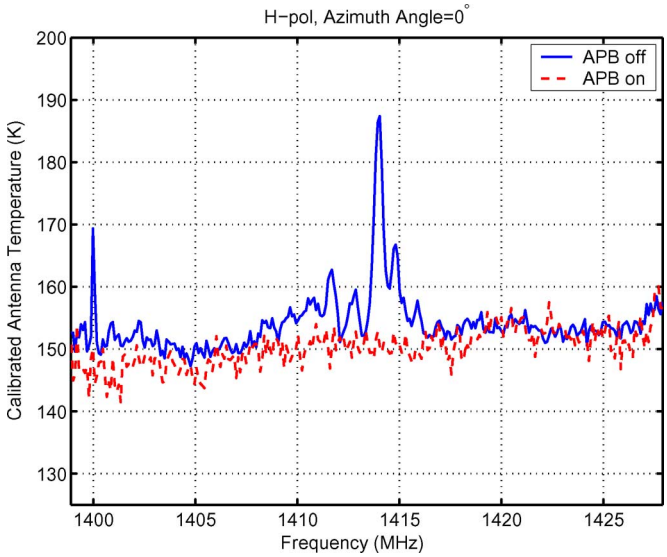

Fig. 4. Average calibrated antenna temperature versus frequency, H-pol, azimuth angle = 0°.

the azimuth angle was 0°. The scene included within the antenna pattern consisted of a nearby forest as well as the sky. Note that "Integration, APB on" and "Integration, APB off" modes were not observed simultaneously: the results shown are an average of data on June 17 from 14:51:43–14:56:15 UTC for "Integration, APB off" mode (around 110 s of antenna observation time) and 14:56:43–14:58:19 UTC time for "Integration, APB on" mode (around 39 s of antenna observation time). Due to the short time delay between the observations, it can be assumed that the natural radiation observed was relatively similar in both cases; note that there is a slight trend of antenna temperatures versus frequency that is consistent with the expected loss properties of the antenna as a function of frequency. The horizontal axis of these figures is the RF frequency, which is mapped from the LISR IF frequencies of 0–50 MHz for the LO frequency of 1440.5 MHz and truncated to the range of 1399–1427 MHz.

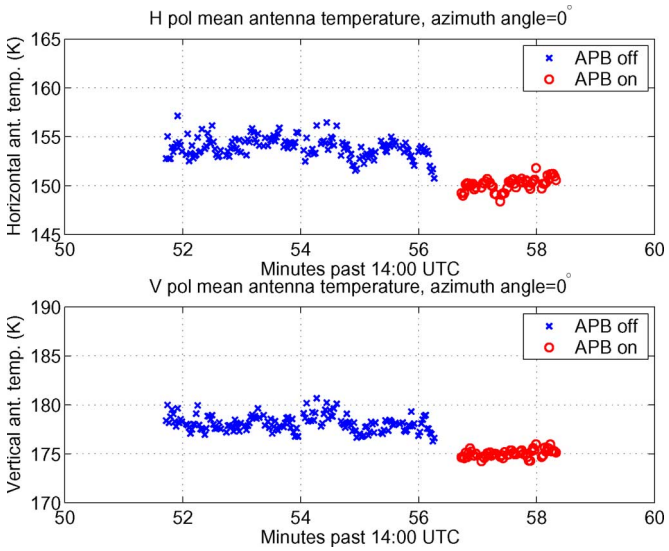

Fig. 5. Calibrated LISR data in the band of 1399–1428 MHz versus time for both APB off and APB on modes when azimuth angle is 0°. The upper plot shows horizontal polarization, and the lower plot shows vertical polarization.

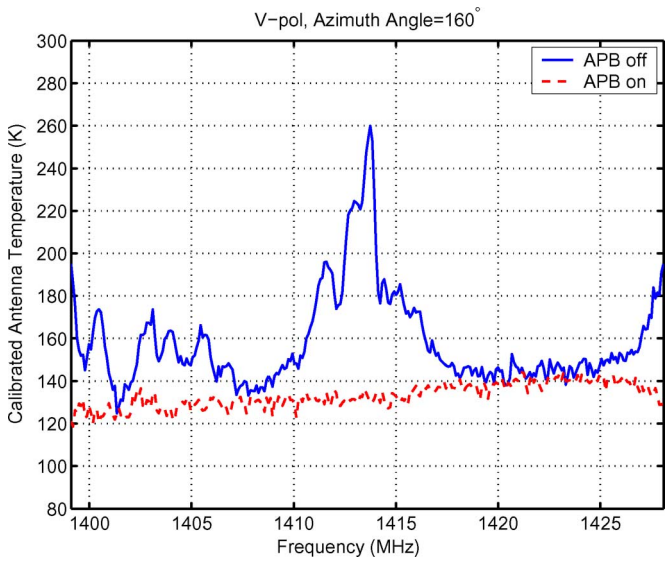

Fig. 6. Average calibrated antenna temperature versus frequency, V-pol, azimuth angle = 160°.

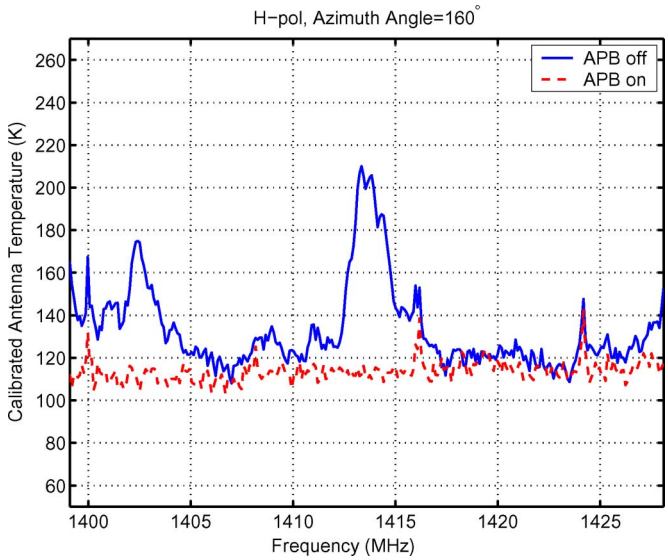

Fig. 7. Average calibrated antenna temperature versus frequency, H-pol, azimuth angle = 160°.

Narrowband emissions near 1400 MHz can be observed for both polarizations; this source is apparently more continuous in nature so that the APB status has only limited impact. The exact origin of this source is not known, although similar emissions have been observed in other campaigns at a variety of locations, suggesting that emissions from some variety of consumer electronics or computer devices may be responsible.

Another strong RFI source in the range of 1410–1415 MHz is observed for both polarizations, which is dramatically reduced in the "Integration, APB on" mode. If 1315-MHz ARSR emissions received by the radiometer antenna due to scattering from the forest scene are insufficiently attenuated by the radiometer front-end filters, the resulting IF frequency is 125.5 or 71.5 MHz for LO frequencies of 1440.5 and 1386.5 MHz, respectively. When sampled at 100 MSPS, these frequencies are mapped to RF frequency of 1415 MHz. Thus, the 1410–1415 RFI source originates from the radar and is successfully mitigated by the APB. The APB processor reported approximately 3% blanking of samples in this case, which is reasonably consistent with a combination of 1.6% that is reported for the internal calibration loads and the 1.4% that results from blanking a 40-μs window at the known radar PRF.

Fig. 5 plots the V- and H-pol total channel antenna temperatures in the band of 1399–1428 MHz versus time for both APB on and APB off modes. Results show the APB on data to have a mean antenna temperature around 3 K that is less than that of the APB off data due to the removal of RFI contributions in the APB on case. The APB on data also exhibit much smaller variations among samples compared to the APB off results. These results show that the APB algorithm is extremely effective in this RFI environment, even with apparently "weak" pulses (RFI contributions comparable to possible geophysical variations and to the antenna temperature's standard deviation) when integrated over time and the radiometer bandwidth.

Figs. 6 and 7 provide the same results when the antenna was looking directly at the radar (i.e., azimuth angle is 160°). The calibrated antenna temperatures shown are an average of observations on June 17 between 15:51:55–15:53:10 for "Integration, APB off" mode and 15:53:40–15:53:58 for "Integration, APB on" mode. Again, the horizontal axis shows the RF frequency that is mapped from the IF frequency, but the LO frequency was 1386.5 MHz in this case. The APB processor reported a similar fraction of samples blanked as in the 0° azimuth angle case.

The level of the antenna temperature in "Integration, APB off" mode is higher than the APB on mode for almost all frequencies, which suggests that pulse amplitudes are sufficiently high to cause some degree of saturation within the digital receiver processing. Continuous RFI sources at 1400, 1417, and 1424 MHz apparently associated to some degree with the radar emissions can be observed for horizontal polarization, which are not strongly affected by the APB.

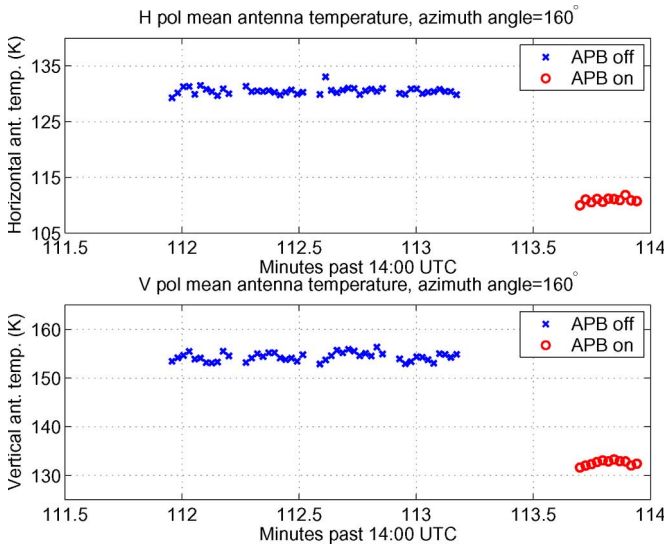

Fig. 8. Same as in Fig. 5, but when azimuth angle is 160°.

The maximum antenna temperature in "Integration, APB off" mode occurs around 1414 MHz for both polarizations and, again, is significantly reduced along with the apparent saturation effects by the APB algorithm. Fig. 8 illustrates the total channel antenna temperatures over an extended time period for this case, showing much larger differences (up to 20 K) between the APB on and off cases than in Fig. 5. While the RFI in this case would be more easily detectable due to the high levels observed, the APB algorithm removes these effects in real time without requiring further processing of data and allows continued observations even in the presence of strong RFI. Note that the remaining narrowband nonpulsed emissions can be removed through the use of the cross-frequency algorithms that are discussed in the next section; such results are shown in [8].

III. Airborne C-Band RFI Measurements and Cross-Frequency Blanking

Frequency-domain blanking of RFI is discussed for data obtained from observations at C-band made from NASA's WB-57 high-altitude aircraft using the polarimetric scanning radiometer C/X band (PSR/CXI) radiometer system of the University of Colorado and the CISR digital backend. These observations were performed during a test flight on August 25, 2005 beginning at Ellington Field, Houston, TX, and including overflights of Dallas and San Antonio, as well as a flight segment over the Gulf of Mexico. Fig. 9 illustrates the geographical region observed and includes UTC flight times along the path. Note that major cities including Houston, Dallas-Fort Worth, and San Antonio are marked with circles.

A. Instrumentation

The PSR/CXI system used for the antenna and front end has been deployed in several previous airborne remote sensing campaigns [3] and provides well-calibrated scene brightness temperature measurements along with a variety of possible scanning patterns during flight operations. The data presented here are from conically scanned operations (i.e., the antenna is rotated in azimuth at a fixed speed) at a fixed incidence angle of 55° from nadir. The antenna at 3-dB beamwidth is approximately 10°. When in conical scan mode, the PSR/CXI antenna rotation period was typically 40 s.

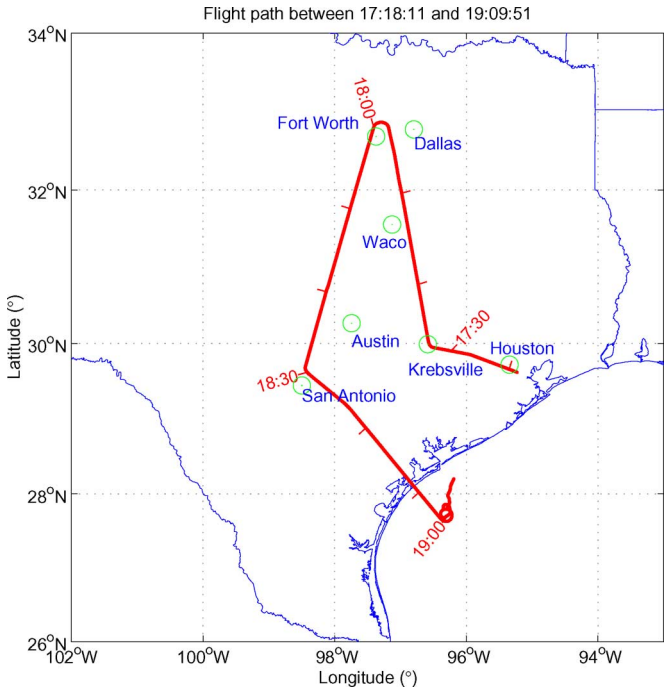

Fig. 9. Flight path, including nearby Texas cities (circles) for the WB-57 campaign.

The PSR/CXI instrument includes four C-band subchannels, with respective frequency ranges of 5.8–6.2, 6.3–6.7, 6.75–7.1, and 7.15–7.5 GHz. The system includes a downconverter module with an image reject mixer to produce 22 tuned 100-MHz channels between 5.5 and 7.7 GHz that are observed by the CISR backend. The LO was swept continuously throughout the flight, with each channel and internal calibration loads being observed for approximately 37 ms; a complete sweep of channels required approximately 814 ms. A portion of the tuned signal for V-pol was coupled to CISR; CISR did not measure H-pol in this experiment. The CISR digital receiver backend measures the incoming signal using two 200-MSPS A/D converters to obtain a 100-MHz sampled signal. The remaining CISR operations starting with the APB are identical to those of LISR. The CISR system used is similar, in general, to that described in more detail in [9], with slight modifications to improve survivability in the high-altitude environment. "Integration, APB off" and "Capture" modes were utilized in this experiment. In the "Integration, APB off" data to be examined here, a base temporal resolution of 1.3 ms was used, with 12 1024-point spectra obtained in 15.75 ms for antenna observations in each tuned channel.

B. Frequency-Domain Mitigation

The WB-57 campaign represents a very dynamic RFI environment, with differing RFI sources observed as the tuned channel is swept through the C-band and as the aircraft location

changes. As shown in Fig. 9, the flight path included major urban centers, rural areas, and the Gulf of Mexico; all of which involve differing RFI properties. Because pulsed sources are not common at C-band, the cross-frequency mitigation method is emphasized here through postprocessing of the measured data. Since naturally emitted thermal noise is expected to vary slowly with frequency, and since CISR has a very high spectral resolution, cross-frequency mitigation should be very effective against RFI that is localized in frequency.

The cross-frequency mitigation technique was applied to calibrated data. A particular observation provides brightness temperatures in 1024 frequency bins of approximately 97 kHz each as a result of the FFT operation. The algorithm operates on a single set of 1024 frequency bins that are averaged to 15.75-ms time resolution as follows:

1) First, an acceptable brightness temperature range is set depending on the scene observed. Frequency bins with brightnesses outside the acceptable range are marked as corrupted. For land observations, the acceptable range was set as 200–400 K.
2) The standard deviation and mean (both over frequency) of brightnesses are found for the lowest 85% (in terms of brightness) of the remaining frequency bins (to avoid bias of the mean and standard deviation by RFI). Another threshold test is then applied: frequency bins that are more than four standard deviations from the mean over frequency are marked as corrupted. Neighboring frequency bins within four frequency bins of the corrupted bins are marked as well.
3) Brightness temperatures of the corrupted bins are replaced with the mean of the remaining frequency bins.

This algorithm is relatively simple compared to other cross-frequency algorithms that have been developed for a smaller number of channels [3], [9]. However, it will be shown to be successful in removing much of the observed RFI in what follows. Simplicity in the algorithm is desirable in order to make future implementation in digital hardware feasible. Because future hardware implementation would likely utilize uncalibrated data, rather than the calibrated data as in the current algorithm, continued work will be required to develop an approach that incorporates power variations with frequency caused by the system passband response.

While it is again possible ideally to predict the false-alarm rate of this algorithm, consideration of the neighboring frequency bins in the cross-frequency blanking process complicates the analysis. A Monte Carlo analysis, however, showed the false-alarm rate for the specified algorithm to be $\approx 2\%$.

As an example of the algorithm's performance, Fig. 10 plots a comparison of unmitigated and mitigated brightness temperatures versus UTC time for CISR channels 8, 12, 16, and 20 during a 1-h portion of the flight (all over land). These total channel brightnesses were calculated by taking the average of the calibrated brightnesses in the 1024 CISR frequency bins corresponding to a 100-MHz bandwidth. Channel 8 represents observations from 6.2 to 6.3 GHz, channel 12 is 6.6–6.7 GHz, channel 16 is 7–7.1 GHz, and channel 20 is 7.4–7.5 GHz. The brightness temperature points shown are averaged over

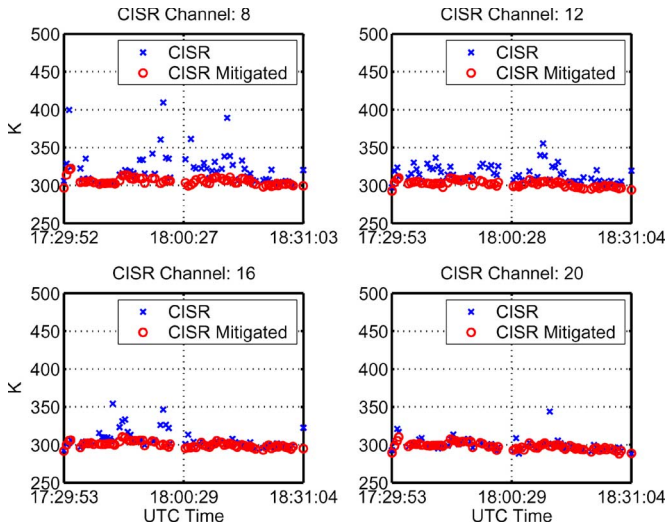

Fig. 10. Comparison of calibrated brightness temperatures versus time between original and mitigated data for CISR channels 8, 12, 16, and 20.

the observations in the specified channel during a 40-s time period; this is equal to one period of the antenna's conical scan. Time periods with no points in the figures correspond to times when the antenna was not in conical scanning mode or when it observed external hot or cold load targets for calibration purposes.

All four of these channels (as well as the CISR channels not plotted) show significant RFI corruption, with brightnesses averaged over 40 s exceeding 400 K in some cases, and the level of RFI corruption shows a significant variation over time. In measurements around 18:00 UTC when the aircraft was over the Dallas-Fort Worth area, all channels show large brightness temperatures. The higher frequency channels show less RFI corruption compared to the lower frequency channels, which is in accordance with the expected higher source densities at lower frequencies. However, all channels show at least 50 K of RFI contributions at some instant during this interval. Results following the application of the cross-frequency mitigation procedure show a greatly reduced impact of RFI. One interesting observation, in general, is that, although all 22 CISR channels were mitigated separately, the mitigated brightnesses are very similar in each channel, as should be expected for thermal noise measurements. Variations of the mitigated temperatures with time are also consistent with expectations for observations over geophysical landscapes.

A more detailed time history of channel 16 (without any averaging of the observed data over time) is presented in the lower half of Fig. 11 for an approximately 90-s portion of the flight over the Dallas-Fort Worth area. As this is an urban scene, it is not surprising that a high degree of RFI activity with an apparent period of ≈ 40 s (the antenna rotation time) can be observed. The mitigation algorithm significantly reduces this RFI. The results also show that portions of the time history without obvious RFI have similar brightnesses before and after the mitigation algorithm. However, RFI mitigations as large as 215 K are observed in some cases. "Spectrogram" images of brightnesses for the original and mitigated data for the same time period are also shown in Fig. 11 (two upper plots).

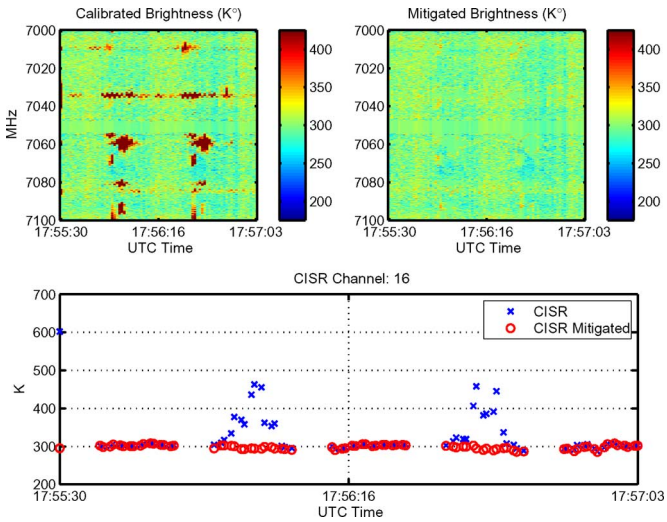

Fig. 11. Spectrogram images and time history of brightness temperatures for original and mitigated data over an urban landscape, CISR channel 16.

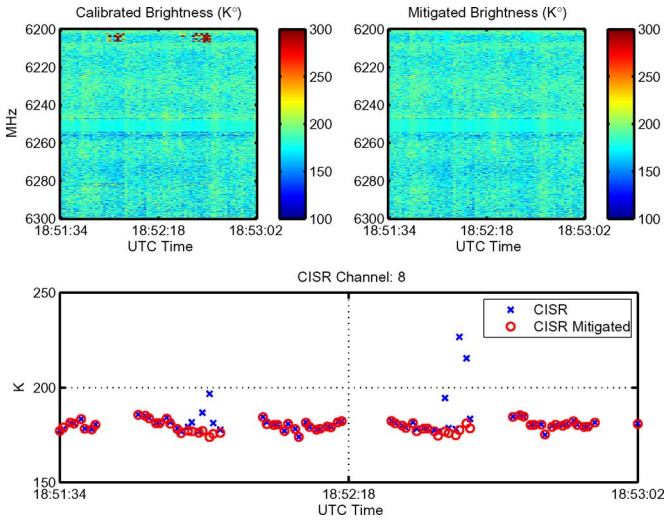

Fig. 12. Spectrogram images and time history of brightness temperatures for original and mitigated data over the Gulf of Mexico, CISR channel 8.

The horizontal axis is the UTC time, and the vertical axis is frequency in megaHertz for these images. The source of the periodic brightness increases in the time-domain plot can be seen clearly here, including apparent sources near 7010, 7040, 7060, 7070, and 7090 MHz. The mitigated data image shows that the algorithm developed removes these contributions.

An example of observations in CISR channel 8 over the Gulf of Mexico is provided in Fig. 12. The plot of total channel brightness versus time (lower plot) is not completely free of RFI even in these at-sea observations. For this case, sources near 6204 and 6282 MHz are successfully mitigated, as shown in the spectrogram images in the upper portion of the figure. Although the contribution of these RFI sources to the total channel brightness is smaller than in the case of observations in the Dallas-Fort Worth area, brightness increases near 45 K can still be observed.

To demonstrate the cross-frequency mitigation performance for weak RFI environments, a 45-s observation over a rural area between Fort Worth and San Antonio is used. A comparison of

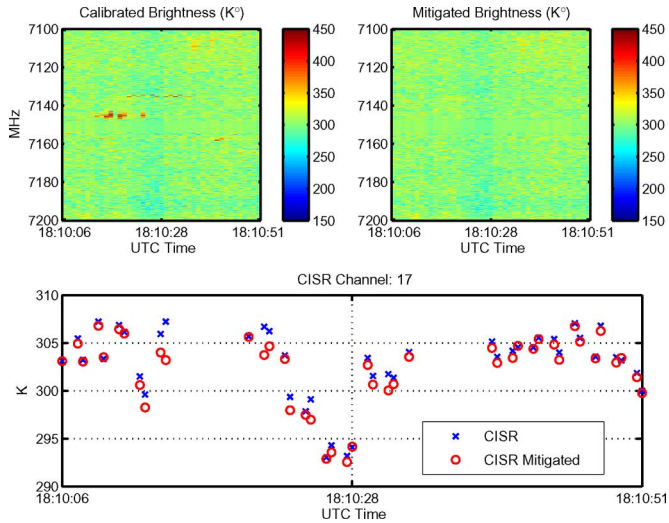

Fig. 13. Spectrogram images and time history of brightness temperatures for original and mitigated data over a rural landscape, CISR channel 17.

original and mitigated data for CISR channel 17 (7.1–7.2 GHz) is provided in Fig. 13, again with the time history of total channel brightnesses in the lower plot and brightness spectrograms in the upper plots. Narrowband interferers around 7107, 7135, 7145, and 7157 MHz are observed in the original brightness image, with 7145 MHz having the largest amplitude; the mitigated image indicates a removal of these sources. The time history plot demonstrates that the contributions of these detected RFI sources to the brightness of the 100-MHz channel are in the range of 1–3 K and comparable to the estimated radiometer brightness standard deviation of 1.5 K. Such low-level RFI is very difficult for a traditional radiometer to detect because it is within the range of the instrument sensitivity as well as within the range of the expected geophysical brightnesses. The high spectral resolution of CISR, however, allows these narrowband but large amplitude sources (i.e., amplitudes more than four standard deviations from the mean brightness over frequency) to be readily detected and removed.

IV. Conclusion

Results from L- and C-band radiometer observations were presented in this paper in order to demonstrate the effectiveness of time- and frequency-domain blanking for RFI mitigation. The L-band Canton campaign included observations in the presence of a pulsed radar system and showed the effectiveness of the real-time APB approach for mitigating pulsed sources. C-band data from an airborne campaign demonstrated that even low-level RFI could be successfully mitigated with a fairly simple cross-frequency blanking algorithm. In both cases, examples were shown in which the use of high time and/or frequency resolution allowed the detection and mitigation of RFI whose signature on larger time or frequency scales was comparable to the instrument sensitivity and expected geophysical variations.

Future campaigns are planned to provide observations over more diverse environments and to allow intercomparison with other RFI mitigation techniques (as already reported in [9]

for a comparison of cross-frequency blanking at low- and high-frequency resolution). Simulations of the expected RFI contributions due to particular sources (as in [15] and [16] for example) can be utilized as well to allow prediction of the expected performance of time and frequency blanking methods. It is hoped that these studies will find application in future air- and spaceborne systems for passive microwave sensing of the Earth.

ACKNOWLEDGMENT

The authors would like to thank Prof. C. Ruf and his team at the University of Michigan for support in the Canton campaign, as well as the PSR/CXI team from the University of Colorado (led by Prof. A. Gasiewski). This work was performed under the sponsorship of a NASA Instrument Incubator Program project (led by the University of Michigan) and the National Polar-Orbiting Operational Environmental Satellite System Integrated Program Office.

REFERENCES

[1] L. Li, E. G. Njoku, E. Im, P. S. Chang, and K. M. St. Germain, "A preliminary survey of radio-frequency interference over the U.S. in Aqua AMSR-E data," *IEEE Trans. Geosci. Remote Sens.*, vol. 42, no. 2, pp. 380–390, Feb. 2004.

[2] S. W. Ellingson and J. T. Johnson, "A polarimetric survey of radio-frequency interference in C- and X-bands in the continental United States using WindSAT radiometry," *IEEE Trans. Geosci. Remote Sens.*, vol. 44, no. 3, pp. 540–548, Mar. 2006.

[3] A. J. Gasiewski, M. Klein, A. Yevgrafov, and V. Leuski, "Interference mitigation in passive microwave radiometry," in *Proc. IEEE Geosci. Remote Sens. Symp.*, 2002, vol. 3, pp. 1682–1684.

[4] M. Basseville and I. V. Nikiforov, *Detection of Abrupt Changes: Theory and Applications*. Englewood Cliffs, NJ: Prentice-Hall, 1993.

[5] P. A. Fridman and W. A. Baan, "RFI mitigation methods in radio astronomy," *Astron. Astrophys.*, vol. 378, no. 1, pp. 327–344, 2001.

[6] C. S. Ruf, S. M. Gross, and S. Misra, "RFI detection and mitigation for microwave radiometry with an agile digital detector," *IEEE Trans. Geosci. Remote Sens.*, vol. 44, no. 3, pp. 694–706, Mar. 2006.

[7] G. A. Hampson, S. W. Ellingson, and J. T. Johnson, "Design and demonstration of an interference suppressing microwave radiometer," in *Proc. IEEE Aerosp. Conf.*, 2004, vol. 2, pp. 993–999.

[8] J. T. Johnson, B. Güner, and N. Niamsuwan, Observations of an ARSR system in Canton, MI with the L-band interference suppressing radiometer, Dec. 2005. project report. [Online]. Available: http://esl.eng.ohio-state.edu/~rstheory/iip/lisr_jtj.pdf

[9] J. T. Johnson, A. J. Gasiewski, B. Güner, G. A. Hampson, S. W. Ellingson, R. Krishnamachari, N. Niamsuwan, E. McIntyre, M. Klein, and V. Y. Leuski, "Airborne radio-frequency interference studies at C-band using a digital receiver," *IEEE Trans. Geosci. Remote Sens.*, vol. 44, no. 7, pp. 1974–1985, Jul. 2006.

[10] J. T. Johnson, A. J. Gasiewski, B. Güner, M. Valerio, and M. Klein, "High altitude measurements of C-band radio frequency interference using a digital receiver," in *Proc. IEEE Geosci. Remote Sens. Symp.*, 2006, pp. 2301–2304.

[11] J. T. Johnson, B. Güner, N. Niamsuwan, and M. Valerio, Airborne C-band RFI measurements with PSR/CXI and CISR from the WB-57 aircraft: Initial data examination, Mar. 2006. project report. [Online]. Available: http://www.ece.osu.edu/~johnson/cisr/cisr060123.pdf

[12] N. Niamsuwan, B. Güner, and J. T. Johnson, "Observations of an ARSR system in Canton, MI with the L-band interference suppressing radiometer," in *Proc. IEEE Geosci. Remote Sens. Symp.*, 2006, pp. 2285–2288.

[13] J. Piepmeier, P. Mohammed, and J. Knuble, "A double detector for RFI mitigation in microwave radiometers," *IEEE Trans. Geosci. Remote Sens.*, 2007. to be published.

[14] N. Niamsuwan, J. T. Johnson, and S. W. Ellingson, "Examination of a simple pulse blanking technique for RFI mitigation," *Radio Sci.*, vol. 40, Jun. 2005.

[15] D. M. LeVine, "ESTAR experience with RFI at L-band and implications for future passive microwave remote sensing from space," in *Proc. IEEE Geosci. Remote Sens. Symp.*, 2002, pp. 847–849.

[16] A. Camps, I. Corbella, F. Torres, J. Bara, and J. Capdevila, "RF interference analysis in aperture synthesis interferometric radiometers: Application to L-band MIRAS instrument," *IEEE Trans. Geosci. Remote Sens.*, vol. 38, no. 2, pp. 942–950, Mar. 2000.

Barış Güner received the B.S. and M.S. degrees in electrical and electronics engineering from Bilkent University, Ankara, Turkey, in 2002 and 2004, respectively.

He is currently a Graduate Research Associate with the Department of Electrical and Computer Engineering, The Ohio State University, Columbus. His current research interests are in microwave remote sensing.

Joel T. Johnson (S'88–M'96–SM'03) received the B.S. degree in electrical engineering from the Georgia Institute of Technology, Atlanta, in 1991, and the M.S. and Ph.D. degrees from the Massachusetts Institute of Technology, Cambridge, in 1993 and 1996, respectively.

He is currently a Professor with the Department of Electrical and Computer Engineering and ElectroScience Laboratory, The Ohio State University, Columbus. His research interests are in the areas of microwave remote sensing, propagation, and electromagnetic wave theory.

Dr. Johnson is a member of commissions B and F of the International Union of Radio Science (URSI), and a member of Tau Beta Pi, Eta Kappa Nu, and Phi Kappa Phi. He received the 1993 Best Paper Award from the IEEE Geoscience and Remote Sensing Society, was named an Office of Naval Research Young Investigator, National Science Foundation Career awardee, and a PECASE award recipient in 1997, and was recognized by the U.S. National Committee of URSI as a Booker Fellow in 2002.

Noppasin Niamsuwan (S'04–M'05) received the B.Eng. degree in electrical and electronic engineering from the Asian University of Science and Technology, Chonburi, Thailand, in 2003, and the M.S. degree in electrical engineering from The Ohio State University, Columbus, in 2005. His Master's thesis is on examination of pulse blanking techniques for digital radiometers. He is currently working toward the Ph.D. degree at The Ohio State University.

His research interests include microwave remote sensing and electromagnetic wave theory. His current research includes scattering models for multilayer rough surfaces.